대한기계학회 2001년도 춘계학술대회논문집 A pp. 26~36

Damage Detection and Suppression in Composites Using Smart Technologies

Nobuo Takeda

Graduate School of Frontier Sciences, The University of Tokyo
c/o Takeda Laboratory, Komaba Open Laboratories (KOL), The University of Tokyo
4-6-1 Komaba, Meguro-ku, Tokyo 153-8904, Japan
TEL/FAX; +81-3-5452-5255, E-mail; takeda@compmat.rcast.u-tokyo.ac.jp

ABSTRACT

Smart sensors and actuators have recently been developed. In this study, first, small-diameter fiber Bragg grating (FBG) sensors developed by the author, whose cladding and polyimide coating diameters were 40 and 52μm, respectively, were embedded inside a laminate without resin-rich regions around sensors and the deterioration of mechanical properties of the composite laminate. The small-diameter FBG sensor was embedded in 0° ply of a CFRP laminate for the detection of transverse cracks in 90° ply of the laminate. The reflection spectra from the FBG sensor were measured at various tensile stresses. The spectrum became broad and had some peaks with an increase of the transverse crack density. Furthermore, the theoretical calculation reproduced the change in the spectrum very well. These results show that the small-diameter FBG sensors have a potential to detect the occurrence of transverse cracks through the change in the form of the spectrum, and to evaluate the transverse crack density quantitatively by the spectrum width.

On the other hand, shape memory alloy (SMA) films were used to suppress the initiation and growth of transverse cracks in CFRP laminates. Pre-strained SMA films were embedded between laminas in CFRP laminates and then heated to introduce the recovery stress in SMA films and compressive stresses in the weakest plies (90° ply). The effects of recovery stresses are demonstrated in the experiments and well predicted using the shear-lag analysis and the nonlinear constitutive equation of SMA films.

1. Transverse Crack Detection in Composites Using Embedded Small-Diameter FBG Sensors

1.1 Background

CFRP composites are used in various fields due to their high specific strength and specific modulus. The failure process of CFRP laminates involves unique microscopic damages, such as transverse cracks and delaminations[1,2]. Especially, transverse cracks in off-axis plies occur at much lower stress than the ultimate tensile strength of the laminates. Hence, it is important to detect the occurrence of the transverse cracks in real-time in order to make practical use of the CFRP laminates effectively and reliably.

A candidate for the sensing device of the transverse cracks is an FBG sensor. Though the sensor is usually used for the measurement of strain or temperature that are almost uniform in the gage length of the sensor[3], that is also very sensitive to non-uniform strain distribution along the entire length of the gratings[4-6]. The strain distribution influences the form of the reflection spectrum from the FBG sensor. Thus, the authors have applied FBG sensors for detecting transverse cracks that cause non-uniform strain distribution in composite materials[7].

However, the cladding of common optical fibers is 125μm in diameter, which is the same as the normal thickness of one ply in CFRP laminates and approximately 20 times larger than the diameter of carbon fibers. Thus, when the normal FBG sensors are embedded into CFRP composites, there exists much possibility that the optical fibers might deteriorate the mechanical properties of the laminates. In order to prevent the deterioration, small-diameter FBG sensors have been recently developed by Hitachi Cable Ltd. and the authors[8]. The outside diameter of polyimide coating is 52 μm, and the cladding is 40μm in diameter. In this research, the small-diameter FBG sensors were applied for the detection of transverse cracks in CFRP composites.

The small-diameter FBG sensor was embedded in 0° ply of a CFRP cross-ply laminate. Then, the reflection spectra from the FBG sensor were measured at various tensile stresses, and the change in the spectrum was investigated. In order to confirm that the change was caused by transverse cracks, the spectra were calculated theoretically. As a result, it was found that the small-diameter FBG sensors have a significant potential to detect the occurrence of transverse cracks through the change in the form of the reflection spectrum, and to evaluate the transverse crack density quantitatively by the spectrum width.

1.2 Experimental Procedure

1.2.1 Materials

Bragg gratings were fabricated in small-diameter optical fibers coated with polyimide layer whose thickness was 6μm. As shown in Fig. 1, the diameters of the cladding and the core are 40μm and 6.5μm, respectively. The transmission loss of the small-diameter optical fiber is 0.5dB/km, and the joint loss with normal optical fibers is about 0.2dB. Furthermore, the tensile strength is about 5.5GPa, which is similar to that of the normal fiber. The schematic structure of the FBG is shown in Fig. 2. The grating length is 10mm, and the grating period is about 0.53μm. The profile of the refractive index modulation was controlled as a cosine function to suppress the side-lobe of the reflection spectrum[8].

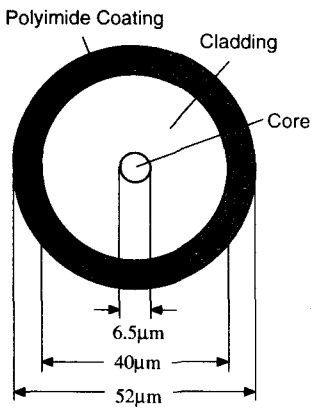

Figure 1. Cross sectional of the small-diameter optical fiber.

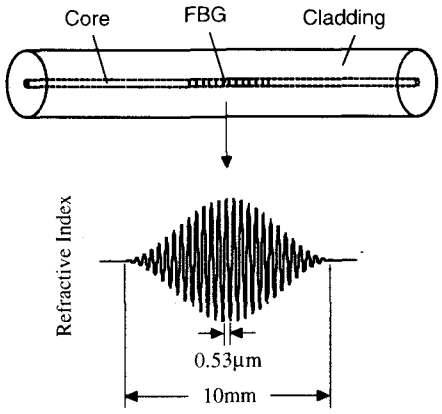

Figure 2. Schematic of the small-diameter FBG sensor.

These FBG sensors were embedded in CFRP composites T800H/3631 (Toray Industries, Inc.). The laminate configuration is cross-ply $[0_2/90_4/0_2]$. Figure 3 shows the cross sections of the CFRP laminates including a normal FBG sensor without resin coating or a small-diameter FBG sensor at 0°/90° interface. The normal FBG sensor was embedded into the slit made in the center of a 0° prepreg sheet during the fabrication process, because the diameter of the cladding is 125μm, which is the same as the thickness of one prepreg sheet. Hence, there remained some matrix rich regions around the normal FBG sensor. On the other hand, the small-diameter FBG sensor was only set between a 0° prepreg sheet and a 90° prepreg sheet during the fabrication process, because the outside diameter of

the sensor was much smaller than the thickness of the prepreg sheet. Nevertheless, the small-diameter FBG sensor was successfully embedded into 0° ply along the reinforcing carbon fibers, and there remained no matrix rich region around the sensor. Thus, embedding of the small-diameter FBG sensors into CFRP composites will not deteriorate the mechanical properties of the composites, since the maximum elongation of the FBG sensor is much larger than that of reinforcing carbon fibers.

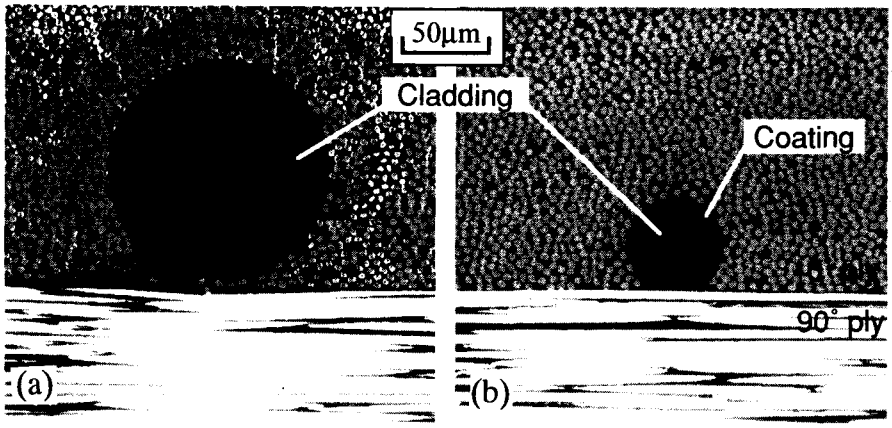

Figure 3. Cross sections of CFRP laminates in which FBG sensors were embedded: (a) a normal FBG sensor without resin coating; and (b) a small-diameter FBG sensor.

As shown in Fig. 4, the FBG sensor is sensitive to the transverse cracks that run through the thickness and width of the 90° ply due to embedment in contact with 90° ply. Moreover, since the optical fiber is embedded in 0° ply to be parallel to the carbon fibers, the optical fiber is hardly broken by the occurrence of transverse cracks in the 90° ply. The geometry and dimensions of the specimen are shown in Fig. 5. In order to avoid the transverse compression load on the embedded optical fiber under tabs when the specimen is held in a testing machine, the optical fiber penetrates through 0° ply perpendicular to the surface of the specimen. This egress method is made possible using the advantage that the small-diameter optical fiber is very fine and flexible. It was assured by tensile tests that the egress point did not induce the fracture of the specimen.

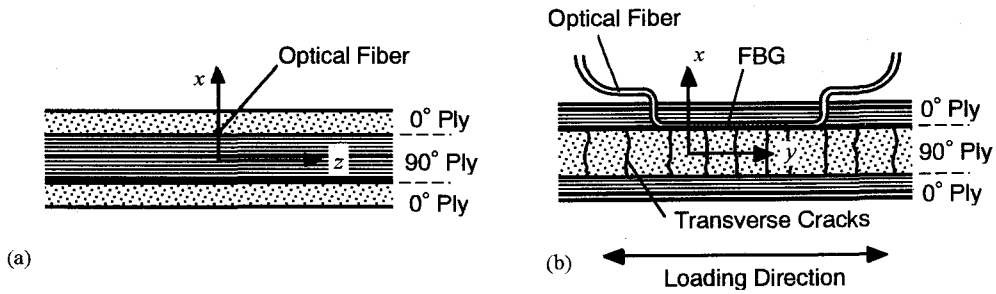

Figure 4. Cross sections of the CFRP laminate including a small-diameter FBG sensor: (a) perpendicular to the loading direction; and (b) parallel to the loading direction.

1.2.2 Measurements

The schematic of the experimental system is shown in Fig. 6. Quasi-static tensile load is applied to the specimen by a material testing system (Instron Corporation, Load Frame 5582) at room temperature. The loading speed is 0.25mm/min. Tensile strain was measured with a strain gage attached on a surface of the specimen, and the tensile load was measured with a load cell. The optical fiber was illuminated by an amplified spontaneous emission (ASE)

light source unit (Ando Electric Co., Ltd., AQ6310(155)), whose wavelength range was more than 40nm. The reflection spectrum was obtained under tensile loading by using an optical spectrum analyzer (Ando Electric Co., Ltd., AQ6317). After that, the tensile load was decreased to 0N, and the reflection spectrum was measured again. Then, the positions and the numbers of transverse cracks in 90° ply were observed at a polished edge surface of the specimen by an optical microscope. This loading/unloading procedure was repeated as the maximum tensile strain was raised, until the specimen fractured completely.

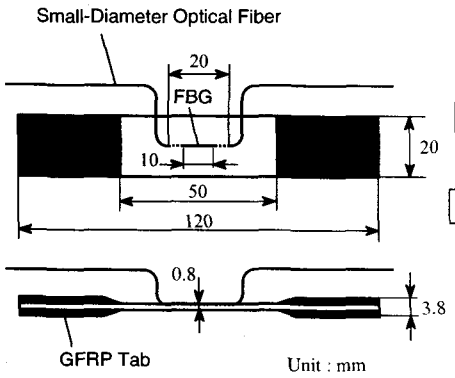

Figure 5. Geometry and dimensions of the specimen.

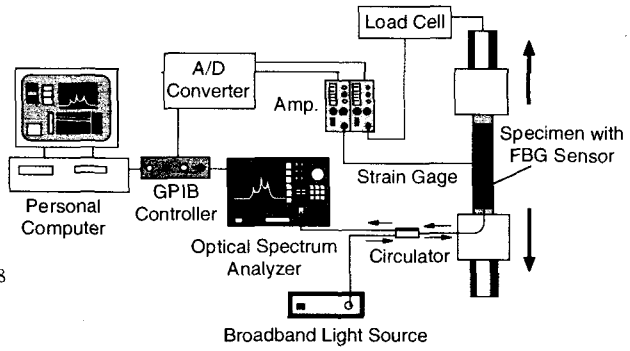

Figure 6. Schematic diagram of the experimental system.

1.3 Experimental Results

Figure 7 shows the tensile stress σ and the crack density ρ measured for the specimen with the embedded small-diameter FBG sensor as a function of the strain ε. The crack density was defined as the number of transverse cracks per unit length along the loading direction in 90° ply.

In Fig. 8, the reflection spectra at various tensile strains are shown. They correspond to the data (A) ~ (E) in Fig. 7. The form of the spectrum before loading (A) is already different from that before embedding owing to transverse thermal residual stresses during the curing process. However, the difference is smaller than that of the normal FBG sensor[7]. While there was no transverse crack, the spectrum kept its shape and the center wavelength shifted corresponding to the strain. After transverse cracks appeared, the form of the reflection spectrum was distorted with an increase in the crack density ρ; the intensity of the highest peak became small, some peaks appeared around it, and the spectrum became broad. Furthermore, reflection spectra measured after unloading are shown in Fig. 9. All spectra recovered their height after unloading. However, the form of the spectrum was not recovered completely after transverse cracks were generated in the laminate.

These changes in the form of the spectrum are expected to be due to the strain distribution caused by the transverse cracks in 90° ply under loading. This will be confirmed through theoretical analysis in the following section.

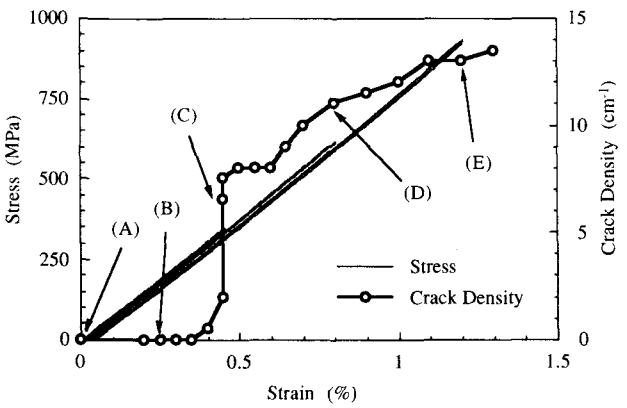

Figure 7. Stress σ and crack density ρ as a function of strain ε.

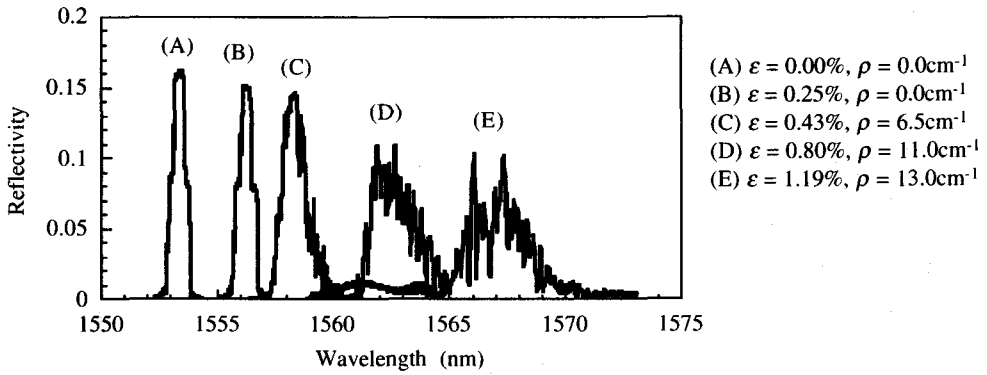

Figure 8. Reflection spectra measured at various values of tensile strain ε. These correspond to the data (A) ~ (E) in Fig. 7.

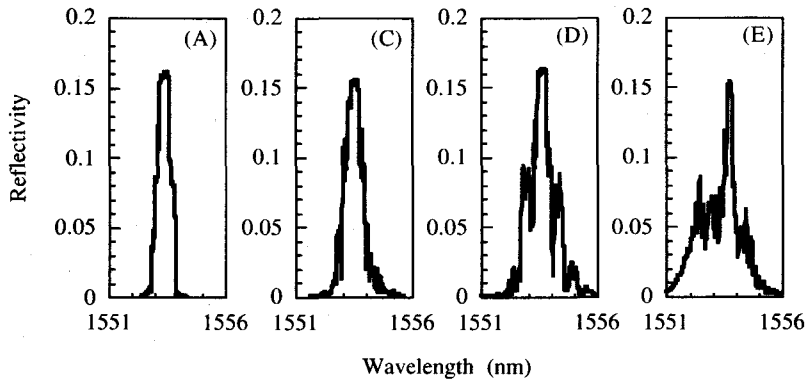

Figure 9. Reflection spectra measured after unloading. These correspond to the spectra at (A), (C), (D), and (E) in Fig. 8.

1.4 Theoretical Analysis and Comparison with Experiments

For confirmation that the change in the spectrum form was caused by transverse cracks, the spectrum was calculated theoretically. In the calculation, it was assumed that the FBG sensor was influenced only by axial strain distribution, and the optical fiber perfectly adhered to the matrix of the 0° ply. Though there is the polyimide coating at the interface, the axial strain distribution in the FBG sensor is assumed to be the same with the longitudinal strain distribution along the loading direction in the 0° ply. The details are described in Ref. 7. The calculated results of reflection spectra under loading and those after unloading are shown in Figs. 10 and 11, respectively. These spectra correspond to those in Figs. 8 and 9.

Though the highest peak of the measured spectrum under loading became small with an increase of tensile strain in the experiment, the calculated spectrum kept its height constant. The main reason for this difference may be the microbending loss of the embedded small-diameter optical fiber caused by the non-uniform strain field in the laminate, because the spectrum recovered its height after unloading as shown in Fig. 9. Since the theoretical calculation did not consider the microbending loss, the height of the calculated spectrum kept constant. However, the calculated results reproduce the change in the form of the spectrum very well. These agreements show that the change in the spectrum is caused by the non-uniform strain distribution due to the occurrence of the transverse cracks. The spectra after unloading are also disturbed because of non-uniform thermal residual strain distribution. These results show that the occurrence of transverse cracks can be detected from the change in the form of the reflection spectrum.

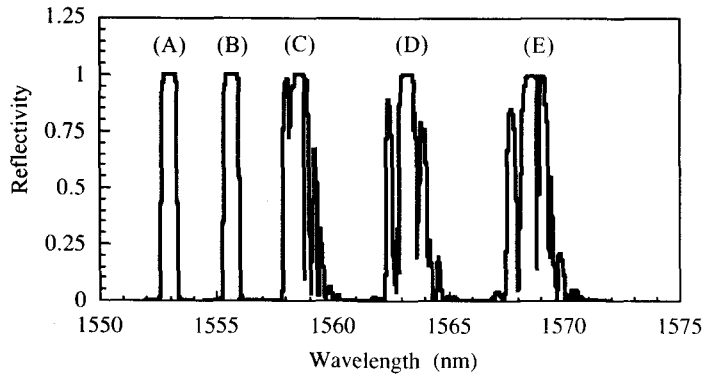

Figure 10. Calculated reflection spectra under loading, which correspond to the measured spectra in Fig. 8.

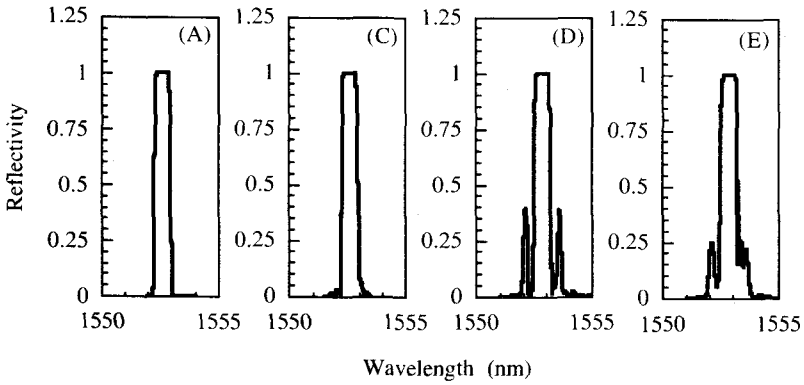

Figure 11. Calculated reflection spectra after unloading, which correspond to the measured spectra in Fig. 9.

1.5 Dependence of Spectrum Width on Crack Density

With increase in the crack density, the width of the reflection spectrum changed in both the experimental result and the theoretical calculation. Thus, the spectrum width and the crack density were plotted as a function of the tensile strain in Fig. 12. The spectrum width was defined as Full Width at Quarter Maximum (FWQM) and normalized by the value before loading. The change of the spectrum width calculated theoretically is smaller than that of the measured spectrum width. This is because the calculated strain in 0° ply is the value averaged through the thickness of the 0° ply, so that the variation of the calculated axial strain is smaller than that of the actual strain of the optical fiber that exists near the crack tip of transverse cracks. Consequently, the calculated spectrum width is smaller

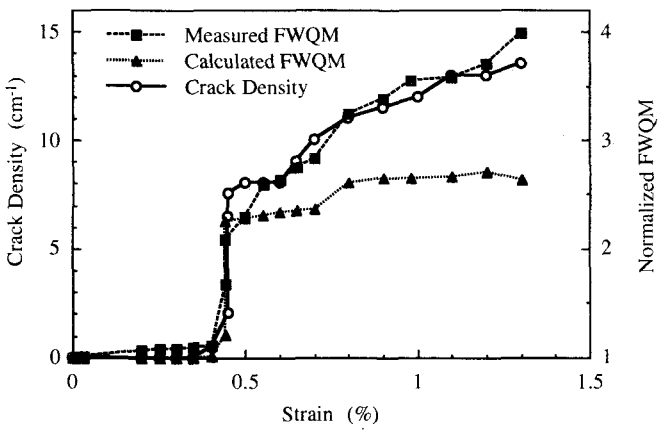

Figure 12. Crack density and spectrum width under loading as a function of tensile strain.

than the actual width. However, both spectrum widths obtained from experiments and theoretical calculation show the same tendency of an increase as the crack density. Thus, the spectrum width has a potential to be a good indicator to evaluate the transverse crack density quantitatively in real time. Moreover, the spectrum width after unloading is plotted in Fig. 13. The change in the spectrum width is reduced after unloading, but some permanent change can be observed.

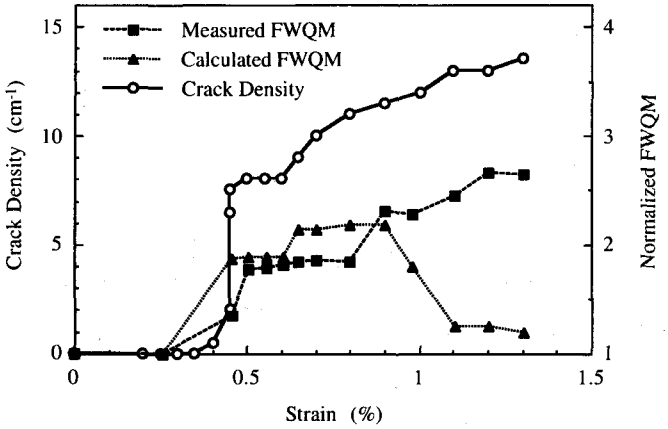

Figure 13. Crack density and spectrum width after unloading as a function of maximum tensile strain.

1.6 Summary

In this research, newly developed small-diameter FBG sensors were applied for the detection of transverse cracks in CFRP cross-ply laminates. The small-diameter FBG sensor could be embedded in 0° ply on the border of 90° ply without matrix rich region. When the tensile load was applied for the specimen, the form of the reflection spectrum from the FBG sensor was distorted sensitively, as the transverse crack density in 90° ply increased.

Then, the reflection spectrum corresponding to the measured one was calculated theoretically. The calculated spectrum reproduced the change in the form of the spectrum both under loading and after unloading very well. From these agreements, it was confirmed that the change in the spectrum was caused by the non-uniform strain distribution, which was induced by the transverse cracks. Hence, the occurrence of transverse cracks could be detected from the change in the form of the reflection spectrum. Furthermore, the spectrum width at the quarter maximum was found to be a good indicator for the quantitative evaluation of the transverse crack density in real time.

2. Transverse Crack Suppression in Composites Using Embedded SMA Films

2.1 Background

Here, a novel method for suppressing the transverse cracking in composite laminates is presented. Shape memory alloy (SMA) films are used to suppress the initiation and growth of transverse cracks in CFRP laminates. Prestrained SMA films are embedded between laminas in CFRP laminates, and then heated to introduce the recovery stress in SMA films and compressive stresses in the weakest plies (90° ply), with the deformation kept by the fixture jig during the fabrication. The concept is illustrated in Fig. 14. The effects of recovery stresses are demonstrated in the experiments and well predicted using the shear-lag analysis and the nonlinear constitutive equation of SMA films.

Improvement of interlaminar shear strength (ILSS) between SMA films and CFRP laminas was attempted in order to obtain the optimum surface treatment through various surface treatment methods such as spattering, sol-gel, ion-plating and anodic-oxidation. A high ILSS was obtained similar to that of CFRP laminates alone. The details can be found in Ref. 9.

2.2 Thermo-mechanical behavior of SMA films

Ti-50.2at.% Ni SMA films (thickness: 0.040mm) were fabricated by Furukawa Electric Co. Ltd. SMA are very

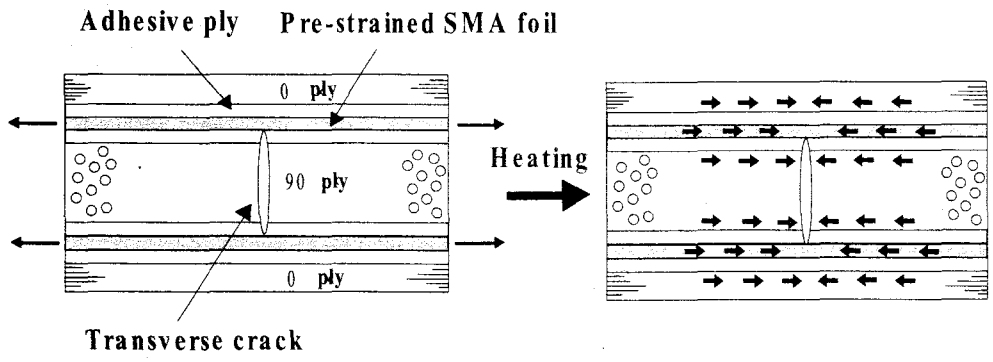

Figure 14. Concept of transverse crack suppression due to recovery stress of SMA films.

sensitive to stress and temperature. Stress-strain curves become quite different depending on the tested temperature as shown in Fig. 15. Load-unload tests at room temperature in Fig.15(b) revealed that the residual strain after unloading was approximately 83% of the maximum applied strain. This residual strain will be recovered when the SMA film is heated above the phase transformation temperature, although the recovery stress will be generated if the deformation is constrained during the heating. The detailed analysis was conducted from the obtained stress-strain-temperature relations and described in Ref. 10. As-fabricated SMA films were in self-accommodation Rhombohedral (SAR) phase without applied stress at room temperature. When the tensile stress was applied, the SMA films was transformed to stress-induced Rhombohedral (SIR) phase by rearrangement of the Rhombohedral phase. With increasing stress, the SIR phase was transformed into stress-induced Martensite (SIM) phase due to Martensite transformation. Both SIR and SIM phases are transformed into Austenite phase when the film are heated above the corresponding phase transformation temperature and have shape memory effects.

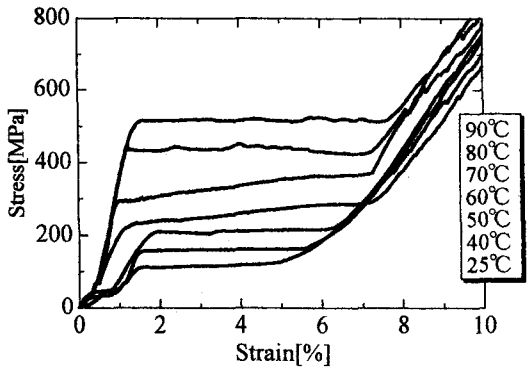

(a) Stress-strain curves at different temperatures

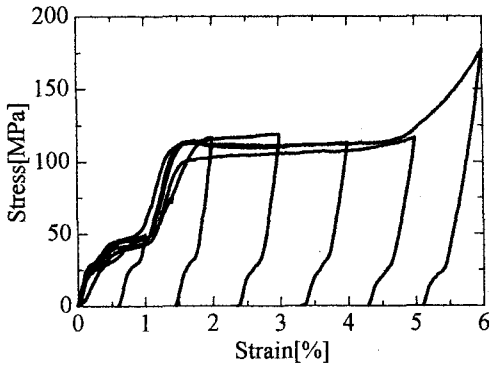

(b) Load-unload stress-strain curves at room temperature

Figure 15. Stress-strain curves of SMA films.

A lot of efforts have been conducted among researchers to model the thermo-mechanical behavior of SMA in recent years. Among them, the Brinson model[11] was adapted in the present study, although the revision was necessary to take into account the Rhombohedral phase. The constitutive equation of the SMA film can be written in the following form[10]:

$$d\sigma_{SMA} = \frac{1}{\left(1+\varepsilon_L^M E(\xi)\frac{\partial \xi_S^M}{\partial \sigma}+\varepsilon_L^R E(\xi)\frac{\partial \xi_S^R}{\partial \sigma}\right)}\left[E(\xi)d\varepsilon-\left\{\varepsilon_L^M E(\xi)\frac{\partial \xi_S^M}{\partial T}+\varepsilon_L^R E(\xi)\frac{\partial \xi_S^R}{\partial T}+\alpha(\xi)E(\xi)\right\}dT\right] \quad (1)$$

where $E(\xi)$, $\alpha(\xi)$ are Young's modulus and thermal expansion coefficient, respectively. ε_S^M, ε_S^R are the maximum

transformation strains, and ξ_S^M, ξ_S^R are the volume fractions. The superscripts M and R denote Martensite and Rhombohedral phases, respectively. The subscript S denotes the stress-induced transformation. The $\xi_S^{M,R}$ is approximated by a cosine function as

$$\xi_S^{M,R} = \xi_S^{M,R}(\sigma, T) \tag{2}$$

$E(\xi)$ and $\alpha(\xi)$ are written in the following forms when parallel models are assumed for the volume fraction.

$$\begin{cases} E(\xi) = \xi^R E_R + \xi^M E_M + \xi^A E_A \\ \alpha(\xi) = \xi^R \alpha_R + \xi^M \alpha_M + \xi^A \alpha_A \end{cases} \qquad \begin{cases} \xi^R + \xi^M + \xi^A = 1 \\ \xi^R = \xi_S^R + \xi_T^R \\ \xi^M = \xi_S^M + \xi_T^M = \xi_S^M \end{cases} \tag{3}$$

The ratio between ξ_S^M and ξ_S^R was determined by curve fitting of the experimental stress-strain curves at room temperature to the theoretical prediction with Eqs. (1)-(3), as shown in Fig. 16.

Then, the general constitutive equations at arbitraty temperatures can be predicted by Eqs. (1)-(3). The calculated recovery stresses of the SMA film are plotted as a function of applied tensile pre-strain in Fig. 17. It is found that the agreement between the experiments and the prediction is reasonablly good.

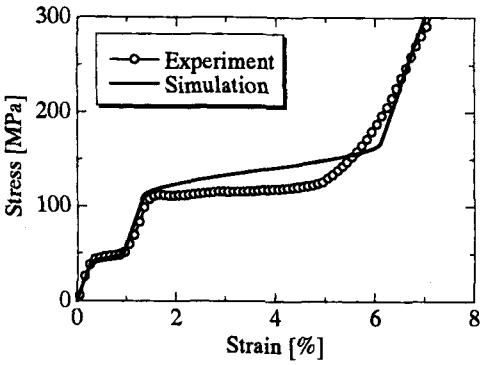

Figure 16. Comparison of stress-strain curves between experiments and the theoretical model.

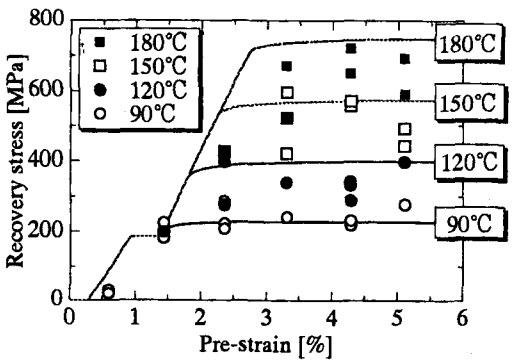

Figure 17. Recovery stresses of SMA films as a function of pre-strain.

2.3 Behavior of CFRP laminates with embedded pre-strained SMA films

Shape memory alloy (SMA) films were used to suppress the initiation and growth of transverse cracks in CFRP laminates. Pre-strained SMA films were embedded between laminas in CFRP laminates and then heated to introduce the recovery stress in SMA films and compressive stresses in the weakest plies (90° ply), with the deformation kept by the fixture jig during the fabrication[10].

A shear-lag analysis was conducted in the present study to predict the transverse crack evolution under tensile loading. The shear-lag model is shown in Fig. 18, where adhesive layers are assumed to transfer the shear stress only. The governing equations including strain-displacement, constitutive and equibrium equations are given in the following:

$$\begin{cases} \varepsilon_1 = du/dx \\ \varepsilon_2 = dv/dx \\ \varepsilon_3 = dw/dx \\ \gamma_{13} = (w-u)/a \\ \gamma_{23} = (w-v)/a \end{cases} \quad \begin{cases} \sigma_1 = E_1(\varepsilon_1 - \alpha_1 \Delta T) \\ \sigma_2 = E_2(\varepsilon_2 - \alpha_2 \Delta T) \\ \sigma_3 = E_3(\varepsilon_3 - \alpha_3 \Delta T) \\ \tau_{13} = G\gamma_{13} \\ \tau_{23} = G\gamma_{23} \end{cases} \quad \begin{cases} b \cdot d\sigma_1 + \tau_{13} dx = 0 \\ d \cdot d\sigma_2 + \tau_{23} dx = 0 \\ s \cdot d\sigma_3 - (\tau_{13} + \tau_{23}) dx = 0 \end{cases} \quad \alpha_3' = \alpha_3 + \frac{\sigma_{SMA}}{E_3 \Delta T} \tag{4}$$

where the recovery stress σ_{SMA} is included in the term of thermal expansion coefficient. These equations are then solved under appropriate boundary conditions when transverse cracks are generated.

Figure 19 shows calculated stress distributions in 90-degree ply at different temperatures. It is found that the

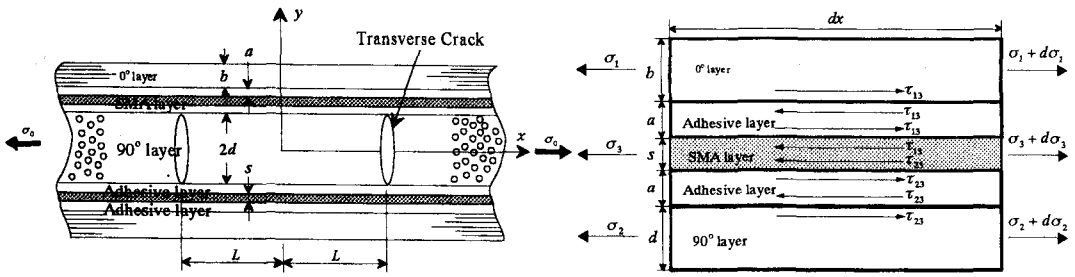

Figure 18. Shear-lag model of SMA-film embedded CFRP laminates.

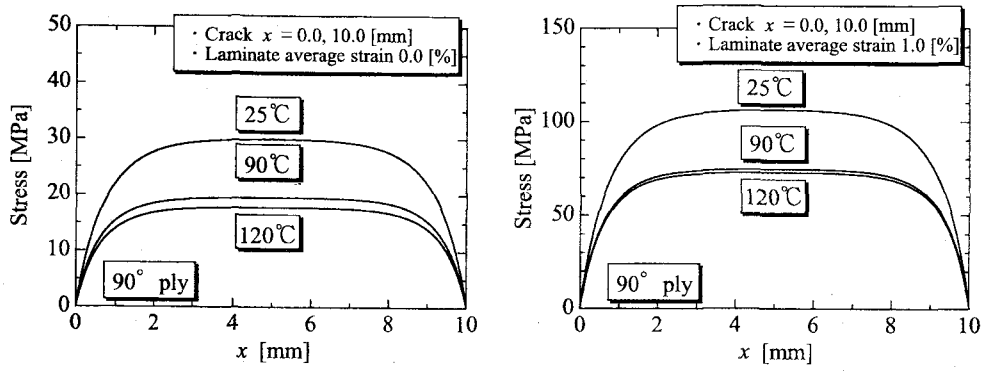

Figure 19. Calculated stress distributions in 90-degree ply at different temperatures. Pre-strain of SMA film= 4%.

temparature increase of the SMA film provides the decrease in stress of the 90-degree ply and suppresses the transverse crack initiation and growth.

Finally, the prediction of the transverse crack initiation and growth was conducted in two different ways. One is the laminate theory considering stochastic strength distribution in 90-degree ply[1]. The other is the Monte-Carlo simulation of the transverse cracking. Comparison of transverse crack density in 90-degree ply between experiments and the theoretical models are given in Fig. 20[10]. The latter prediction provides a better approximation.

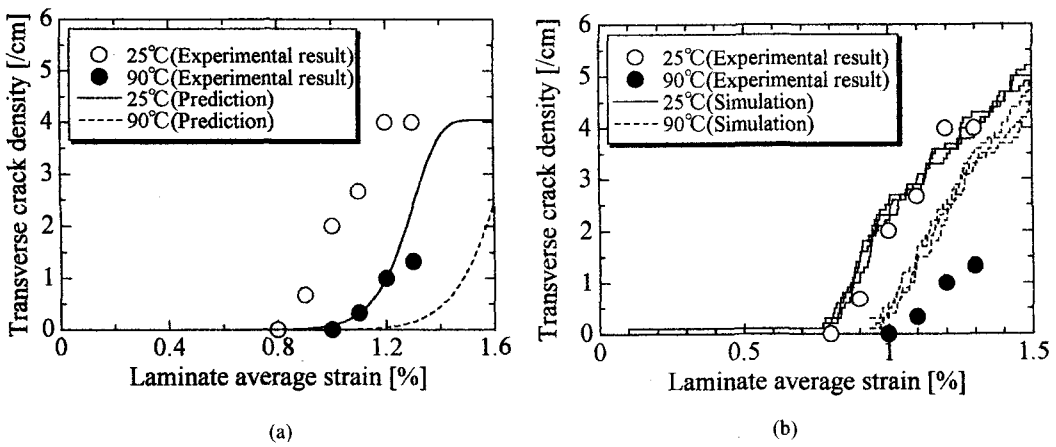

Figure 20. Comparison of transverse crack density in 90-degree ply between experiments and the theoretical model. Pre-strain of SMA film= 4%. (a) laminate theory considering stochastic strength distribution in 90-degree ply and (b) Monte-Carlo simulation

2.4 Summary

SMA films were used to suppress the initiation and growth of transverse cracks in CFRP laminates. Pre-strained SMA films were embedded between laminas in CFRP laminates and then heated to introduce the recovery stress in SMA films and compressive stresses in the 90° ply. The effects of recovery stresses were demonstrated both in the experiments and the theoretical prediction. The transverse crack evolution was also well predicted by combining the shear-lag analysis and the nonlinear constitutive equation of SMA films.

ACKNOWLEDGEMENTS

This research was conducted as a part of the "R&D for Smart Materials Structure System" project within the Academic Institutions Centered Program supported by NEDO (New Energy and Industrial Technology Development Organization), Japan.

REFERENCES

1. N. Takeda and S. Ogihara, "In situ observation and probabilistic prediction of microscopic failure processes in CFRP cross-ply laminates," *Compos. Sci. Technol.*, **52**, pp. 183-195, 1994.
2. N. Takeda and S. Ogihara, "Initiation and growth of delamination from the tips of transverse cracks in CFRP cross-ply laminates," *Compos. Sci. Technol.*, **52**, pp. 309-318, 1994.
3. A. D. Kersey, M. A. Davis, H. J. Patric, M. LeBlanc, and K. P. Koo, "Fiber grating sensors," *J. Lightwave Technol.*, **15**, pp. 1442-1463, 1997.
4. S. Huang, M. M. Ohn, M. LeBlanc, and R. M. Measures, "Continuous arbitrary strain profile measurements with fiber Bragg gratings," *Smart Mater. Struct.*, **7**, pp. 248-256, 1998.
5. K. Peters, P. Pattis, J. Botsis, and P. Giaccari, "Experimental verification of response of embedded optical fiber Bragg grating sensors in non-homogeneous strain fields," *Opt. Laser. Eng.*, **33**, pp. 107-119, 2000.
6. J. A. Guemes, S. Diaz-Carrillo, and J. M. Menendez, "Measurement of strain distribution in bonded joints by fiber Bragg gratings," *Smart Structures and Materials 1998: Sensory Phenomena and Measurement Instrumentation for Smart Structures and Materials*, SPIE Vol. 3330, pp. 264-271, 1998.
7. Y. Okabe, S. Yashiro, T. Kosaka, and N. Takeda, "Detection of transverse cracks in CFRP composites using embedded fiber Bragg grating sensors," *Smart Mater. Struct.*, **9**, pp. 832-838, 2000.
8. K. Satori, Y. Kurosawa, A. Hongo, and N. Takeda, "Development of small-diameter optical fiber sensors for damage detection in composite laminates," *Smart Structures and Materials 2000: Sensory Phenomena and Measurement Instrumentation for Smart Structures and Materials*, SPIE Vol. 3986, 2001 (in printing).
9. T. Ogisu, N. Ando, J. Takaki, T. Okabe and N. Takeda, "Improved surface treatment of SMA foils and damage suppression of SMA-foil embedded CFRP laminates," *Proc. 11th Int. Conf. Adaptive Structures and Technologies, Elsevier*, pp. 261-268, 2001.
10. M. Kobayashi , "Suppression of microscopic damage in CFRP laminates with embedded shape memory alloy films", M.E. thesis, The University of Tokyo, 2001 (in Japanese).
11. L. C. Brinson, "One-dimensional constitutive behavior of shape memory alloys: Thermomechanical derivation with non-constant material functions and redefined martensite internal variables", *J. Intelligent Mater. Systems Struc.*, **4**, pp. 229-242, 1993.